The NASA-JAXA Global Precipitation Measurement mission – part II: New frontiers in precipitation science

The NASA-JAXA Global Precipitation Measurement mission – part II: New frontiers in precipitation science

Daniel Watters[1,2] and Alessandro Battaglia[1,2,3]

[1]*Earth Observation Science Group, Department of Physics and Astronomy, University of Leicester, UK*
[2]*National Centre for Earth Observation, University of Leicester, UK*
[3]*DIATI, Politecnico di Torino, Italy*

GPM applications

Part I of this article details how the Global Precipitation Measurement (GPM) mission (Hou *et al*., 2014; Skofronick-Jackson *et al*., 2017; 2018; Kidd *et al*., 2020) addresses the challenge of global observations of precipitation from a spaceborne perspective (Watters and Battaglia, 2020). In particular, the article highlights the advances in precipitation science provided by the Dual-frequency Precipitation Radar (DPR) and the GPM Microwave Imager (GMI) on-board the GPM Core Observatory (CO), and the passive microwave radiometers on-board each of the GPM constellation of international satellites. The second part of this article progresses onto applications of GPM measurements that epitomise the highlights of the mission. Two applications are outlined: the case study of Hurricane Irma and GPM's global precipitation climatology.

The case study of Hurricane Irma

Advanced precipitation sensors on-board the GPM-CO can help improve our understanding of precipitation systems (Houze Jr *et al*., 2015). The following section explores one application of GPM to study Hurricane Irma in autumn 2017. This study uses the global-gridded Integrated Multi-satellitE Retrievals for GPM (IMERG) precipitation product (Huffman *et al*., 2019a, 2020), the GPM-CO Combined Radar-Radiometer (CORRA or DPR-GMI) precipitation product (Olson *et al*., 2016; Grecu and Olson, 2020) and the Goddard Convective-Stratiform Heating (CSH) latent heat product (Lang and Tao, 2018). The CSH latent heat product is generated using CORRA data (conditional surface rainfall intensity, echo top height, low-level reflectivity gradients, stratiform fraction and surface type) as input for latent heat look-up tables generated by cloud resolving model simulations (Lang and Tao, 2018). The data from these version-6 IMERG, CORRA and CSH products are available at Huffman *et al*. (2019b), Olson (2017) and GPM Science Team (2017), respectively.

Figure 1 depicts the precipitation accumulation of Hurricane Irma, from the formation of the tropical oceanic depression to its dissipation over south-eastern USA. IMERG precipitation estimates from each half-hour in the period provide the accumulation, while the National Oceanic and Atmospheric Administration (NOAA) provides the tropical cyclone path and hurricane category (Knapp *et al*., 2010, 2018). GPM shows that large precipitation amounts were associated with the hurricane phase, especially where the winds were greatest (i.e. category 3 and above). The combination of the IMERG and NOAA datasets shows the ability to understand how changes in strength and location of the hurricane correspond with the precipitation amounts.

A GPM-CO overpass of Hurricane Irma is also depicted in Figure 1, with the swaths of the DPR and GMI's measurements highlighted (see the magenta lines). The DPR and GMI measurements during overpasses provide information into the three-dimensional structures of precipitation, the microphysics of the precipitation (i.e. the type of precipitation, size and number of particles) and the vertical distribution of latent heat release.

Figure 2 shows surface precipitation rate and latent heat estimates of Hurricane Irma corresponding to the time of the GPM-CO overpass shown in Figure 1. Irma had reached the highest hurricane category when the GPM-CO passed over, capturing the eyewalls and rainbands around the hurricane eye. The instruments measured a peak surface rain rate of 146mmh^{-1}, and calculated the latent heat released at 3km (7km) peaking at 37Kh^{-1} (43Kh^{-1}). The precipitation rates from the combined GPM-CO instruments (CORRA) product and global-gridded satellite constellation IMERG product are very similar for two reasons: (1) the GMI instrument provided rainfall estimates which were gridded to half-hour resolution and 0.1 degrees for the IMERG product, and (2) the IMERG precipitation estimates are calibrated to the CORRA product (Huffman *et al*., 2019a). The polarity of

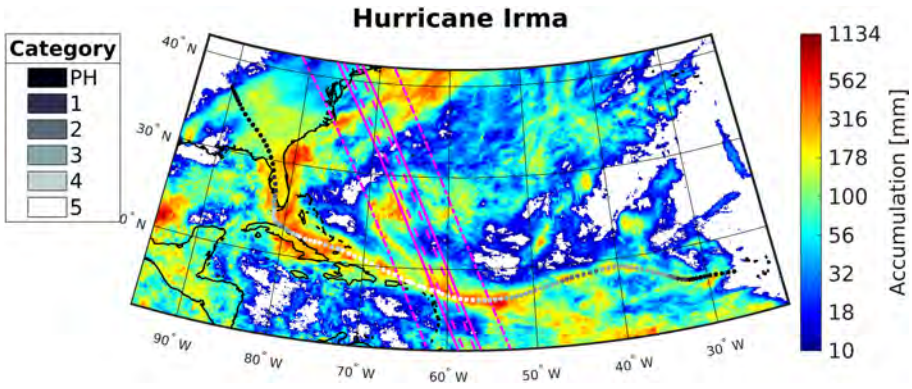

Figure 1. A GPM study of Hurricane Irma, which formed on 30 August 2017 (0000 UTC) before dissipating on 13 September 2017 (1200 UTC). The background colours represent the precipitation accumulation provided by the IMERG product in this period. The dot positions represent the 3-hourly location of Irma's centre, and the dot colours represent the Saffir-Simpson Hurricane Wind Scale Category from the NOAA International Best Track Archive for Climate Stewardship (IBTrACS) v04r00 product. Note that category 'PH' stands for pre/post hurricane status. The magenta tracks represent correspond to an overpass of the GPM-CO; the dashed, solid and dashed-dotted lines represent the DPR Ka-band, Ku-band and GMI swaths, respectively.

RMetS Royal Meteorological Society

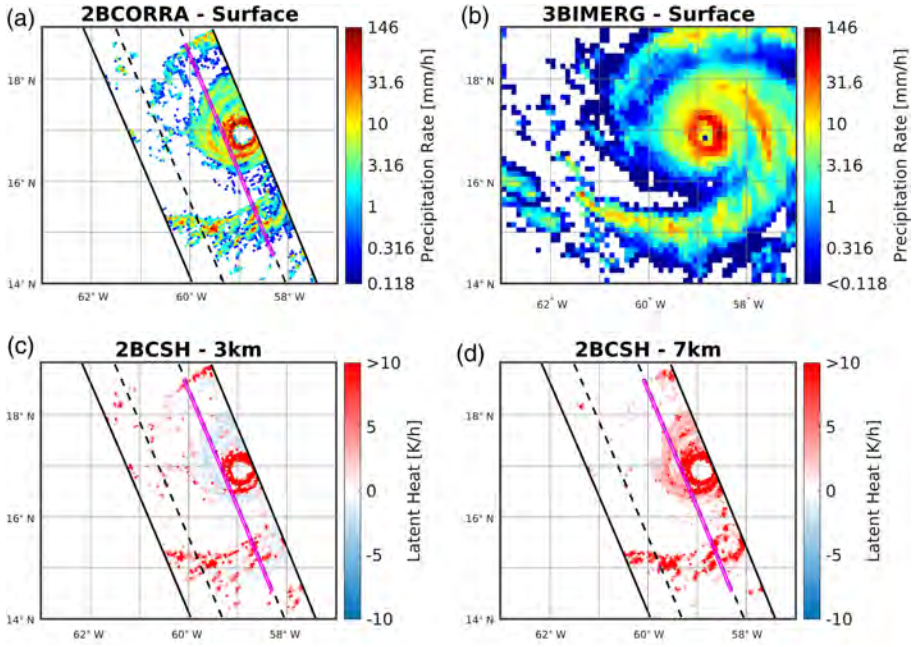

Figure 2. Surface rain rate estimates of Hurricane Irma, from (a) the CORRA product and (b) the IMERG product, and latent heat estimates at (c) 3km and (d) 7km from the CSH product, when the GPM-CO passed over on 5 September 2017 (165046–165211 UTC, granule 20007). The magenta box in panels a, c and d outlines the along-track transect of the cross-section shown in Figure 3. This overpass corresponds to the magenta lines in Figure 1.

the latent heat estimates (whether positive for heating, or negative for cooling) either side of the ~5km freezing level highlight regions of stratiform (uniform and weaker) and convective (non-uniform and stronger) precipitation within the hurricane. Heating at all levels signifies convective regimes, while cooling in the lower troposphere and heating in the upper troposphere signifies stratiform regimes (see Figure 3, and figure 3 of Houze, 1997). The heating rates at 3km reveal the central eyewall and separated rainbands to be convective while most of the surrounding eyewalls are stratiform.

The DPR nicely captures the vertical structure of Hurricane Irma during the overpass of the GPM-CO. Figure 3 depicts the transect corresponding to the elongated magenta box in Figure 2. The DPR's Ku-band measurements and precipitation rate estimates (panels a and c) show precipitation structures that exceed 10km in height, with the reflectivity profile clearly highlighting regions of stratiform and convective precipitation (rectangular and oval boxes, respectively). The precipitation rates show convective precipitation to be much more intense than stratiform precipitation. In terms of radar reflectivity factors, a key signature of stratiform precipitation is the 'bright band' – where the reflectivity factor suddenly increases to a maximum below the freezing level due to melting ice particles. The reflectivity factors tend to be high in the melting region, which is typically around 0.5km in depth, because ice particles may be quite large (compared with raindrops; Houze Jr, 1997) and the radar backscatter of a melting ice particle with liquid water on its extremities exceeds that of its liquid equivalent. The reflectivity is lower below the melting layer because raindrops are smaller and have faster fall speeds than ice particles so that the concentration of particles below the layer is reduced (Houze, 1997). A further reduction in the reflectivity factor below the melting layer is a signature of evaporation of raindrops. A 'bright band' is not commonly found in convective precipitation echoes because stronger updrafts allow precipitation particles to grow to larger sizes before their fall speeds overcome the updrafts at many different vertical levels; this results in a much thicker mixed-phase layer that can extend over several kilometres (Houze Jr, 1997), and typically prevents a clear melting layer from forming.

The Ku- and Ka-band dual-frequency ratio (DFR, panel b), that is, the ratio (difference) between Ku- and Ka-band radar reflectivity factors in linear mm^6m^{-3} (logarithmic dBZ) units, shows that the reflectivity factors at Ka-band are typically smaller. This is a consequence of non-Rayleigh effects on backscattered radiation. In the Rayleigh regime, where the wavelength of incident radiation is much greater than the characteristic size of precipitation particles, the reflectivity factor is proportional to the sixth power of the size. However, in the non-Rayleigh regime where the wavelength is similar to the size of the target, the reflectivity factor is proportional to a smaller power of the particle size than in the Rayleigh regime. This explains why reflectivities are typically smaller at Ka-band (8.5mm wavelength) than at Ku-band (22mm wavelength). The DFR is indicative of the mass-weighted mean raindrop size, with larger DFRs signatures of larger precipitation particles. Panel (b) shows that precipitation particles uniformly increase in size from the top of the storm to the freezing level in stratiform regimes, while particles are large at all levels above the freezing level in the convective column. In both regimes, particles are much smaller below the freezing level because ice particles intersperse into smaller raindrops upon melting. Curiously, raindrops smaller than 1mm tend to produce slightly negative DFR, a phenomenon which is due to a unique resonance feature at Ka-band that produces backscattering cross sections exceeding the Rayleigh reference values (Liao and Meneghini, 2011). Latent heat estimates (panel d) highlight the characteristic S-shape vertical profile of latent heat for stratiform precipitation with cooling below the freezing level and heating above. Furthermore, the convective column is shown to heat the atmosphere at all levels and at a greater magnitude than any stratiform heating or cooling.

Figure 4 depicts the three-dimensional precipitation distribution from Hurricane Irma during the GPM-CO's overpass in this case study. The observations clearly show the central eyewall (red isosurface) and an outer eyewall (blue isosurface), with maximum precipitation found within the central eyewall. A NASA video of the satellite overpasses and hurricane precipitation features is available (https://www.youtube.com/watch?v=Yntg6as94b8).

Global precipitation climatology

The Tropical Rainfall Measuring Mission (TRMM; Simpson *et al*., 1996; Kummerow *et al*., 1998) and GPM constellation's state-of-the-art precipitation sensors provide a 20-year legacy of global precipitation measurements. To highlight the advancements in precipitation science provided by the TRMM and GPM missions, the 20-year IMERG climatological record is compared to three different climatologies. These different climatologies are provided by the Deutscher Wetterdienst (DWD) Global Precipitation Climatology Centre (GPCC; Schneider *et al*., 2014), the Global Precipitation Climatology Project (GPCP; Adler *et al*., 2003, 2018), and the European Centre for Medium-Range Weather Forecast's (ECMWF) ReAnalysis 5 (ERA5; Hersbach *et al*., 2020). The data products are available from Huffman *et al*. (2019b,c; IMERG), Meyer-Christoffer *et al*. (2018; GPCC), Wang (2018; GPCP) and Copernicus Climate Change Service (2017; ERA5). The GPCC Precipitation Climatology

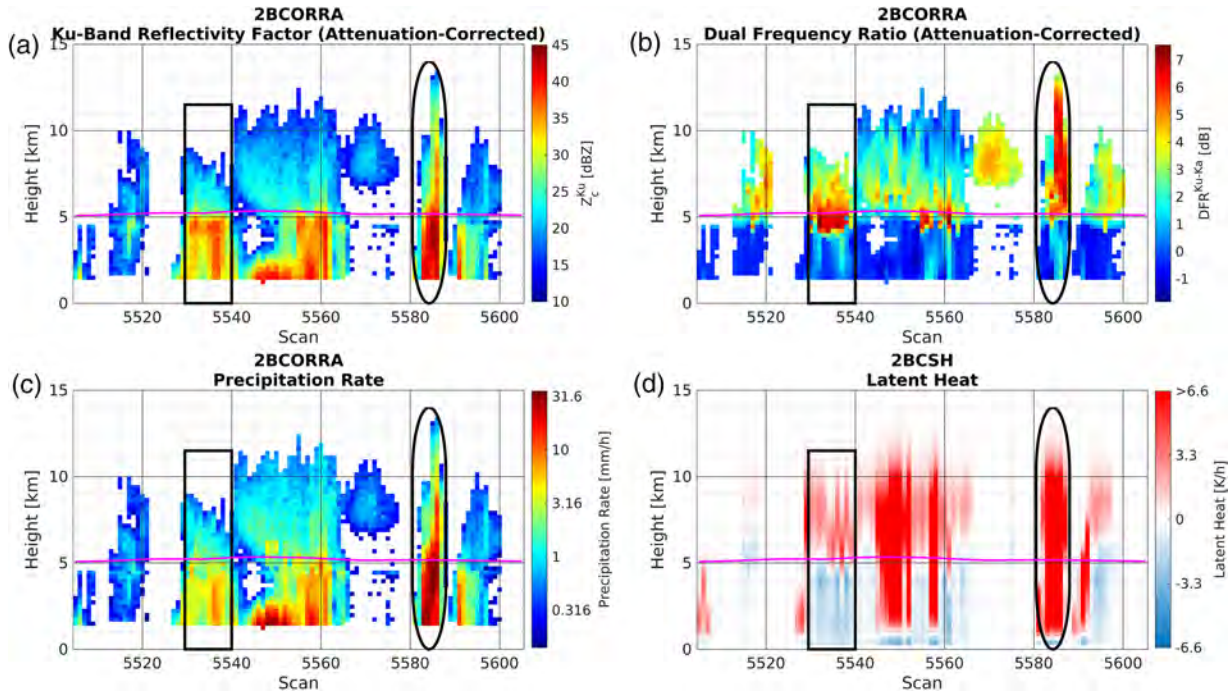

Figure 3. Attenuation-corrected (a) Ku-band radar reflectivity factor, (b) the dual-frequency ratio (i.e. the difference in radar reflectivity factors in dBZ units between the Ku-band and Ka-band), (c) precipitation rate estimates and (d) latent heat estimates from an along-track transect (see the magenta box in Figure 2(a), (c) and (d)) of GPM measurements. The CORRA algorithm produced the attenuation-corrected radar reflectivity factors and the precipitation rate estimates, and the CSH algorithm produced the latent heat estimates. The magenta line in each panel corresponds to the freezing level (from the CORRA product), and the rectangular and oval boxes outline a case of stratiform and convective precipitation, respectively.

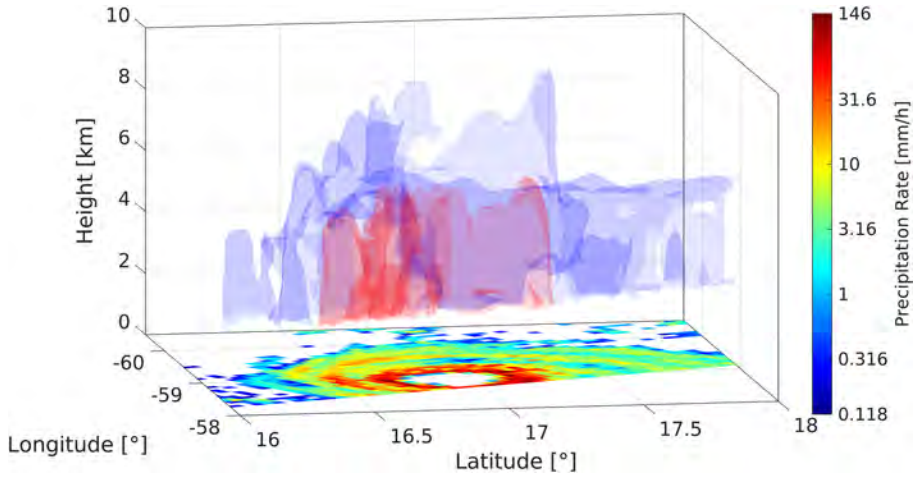

Figure 4. The three-dimensional structure of precipitation from Hurricane Irma, provided by the CORRA product from DPR and GMI measurements made as the GPM-CO passed over the system. The colour bar refers to the surface rain rates (as in Figure 2a), while the blue and red isosurfaces represent 2mmh^{-1} and 13mmh^{-1}, respectively.

Version 2018 product provides climatological precipitation estimates from around 80 000 gauge stations with a minimum of 10 years of measurements (mainly in the period 1951–2000). The GPCP V2.3 Combined Precipitation Data Set provides monthly precipitation estimates from 1979 to near-present, produced from GPCC rain gauge analyses over land, satellite measurements over land and ocean, and sounding observations. ERA5 provides monthly precipitation estimates, produced by data assimilation of models and observations.

Figure 5 depicts the IMERG annual precipitation means (panel a), and their comparisons to the other climatologies (panels b–d). In agreement with previous findings, the regions that experience the most rainfall reside in the Intertropical Convergence Zone (ITCZ) and the South Pacific Convergence Zone (SPCZ). Arid regions include North Africa and the extratropical Pacific (Atlantic) Ocean regions west of North and South America (Africa). IMERG is most similar to the GPCP satellite-gauge product over land, with the largest relative differences found over North Africa's arid Sahara Desert; this is not surprising as the microwave input to the IMERG product is intercalibrated to CORRA, which is calibrated seasonally to GPCP V2.3 over tropical land (Huffman *et al*., 2019a). IMERG's calibration reference, CORRA, is also calibrated seasonally to GPCP V2.3 over high-latitude oceans (Huffman *et al*., 2019a); surprisingly, IMERG is found to estimate more (less) precipitation south of 45°S over the Pacific Ocean (Atlantic and Indian Oceans). IMERG also estimates more precipitation over most of the ocean compared to the GPCP satellite-gauge product, though estimates less in some arid regions close to the west coasts of North and South America, and Southern Africa. Compared to the GPCC gauge product, IMERG estimates more precipitation over most land regions with larger differences mostly found in regions where IMERG estimates precipitation is less than 2mmd^{-1} (Europe, Asia and North Africa). However, IMERG is in close agreement with GPCC gauge-derived precipitation over some regions such as Canada, South America (away from the coastlines), South and Central Africa, Spain, China and Eastern Australia. Whereas IMERG typically estimates more precipitation relative to the GPCC gauge product and the GPCP satellite-gauge product, estimates of less precipitation compared to ERA5 are more prevalent. IMERG tends to compare more favourably to ERA5 than the GPCP satellite-gauge product over ocean; however, ERA5 (as well as GPCP) also consistently estimates less precipitation

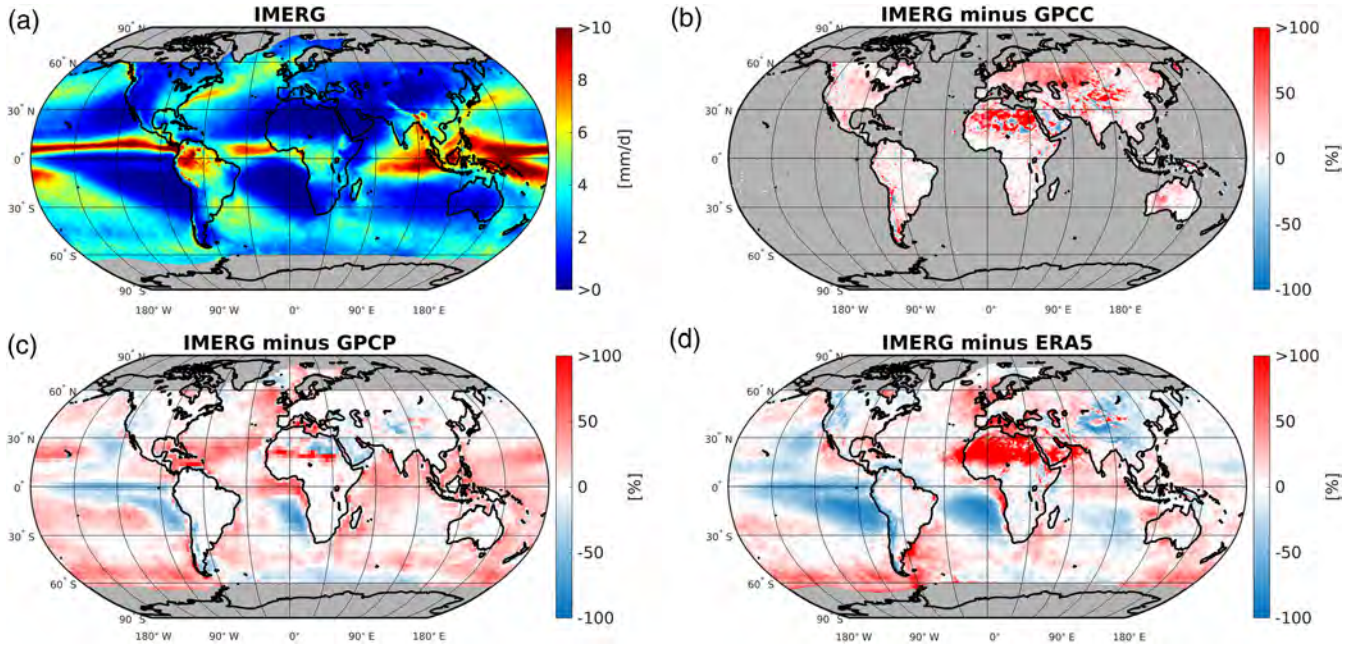

Figure 5. (a) Annual mean accumulation of precipitation from the IMERG V06B product at 0.1°×0.1° resolution for 1 June 2000 to 31 May 2020 (final run data for 1 June 2000 to 31 January 2020, late run data for 1 February 2020 to 31 May 2020). Differences in mean accumulations between the 20-year IMERG product and: (b) the GPCC Climatology Version 2018 product at 0.25° ×0.25° resolution (period: 1951–2000); (c) the GPCP Version 2.3 Combined Precipitation Data Set product at 2.5°×2.5° resolution (period: January 1979 to December 2019); (d) the ERA5 reanalysis product at 0.25°×0.25° resolution (period: January 1979 to December 2019). Differences are normalised by the non-IMERG product. Grey colours highlight regions without estimates from the respective products, and irregular half-hourly estimates (for <80% of the period) by IMERG.

than IMERG in the high-latitude Southern Pacific Ocean and the ocean surrounding Great Britain and Ireland. Over land, IMERG is in good agreement with ERA5 in wet regions; interestingly, ERA5 suggests that IMERG estimates less precipitation along the west coasts of the American continents to a greater extent than the GPCP satellite-gauge product. Overall, the discrepancies between IMERG and the other credible climatologies are an indication of the precipitation climatology uncertainties. The regions where discrepancies are largest (including arid regions, Asia, high-latitude Southern Pacific Ocean, ocean surrounding Great Britain and Ireland) are those that must continue to be studied in order to reduce such climatological uncertainties.

Conclusion

Two examples of GPM measurements are depicted and discussed in this article: the case study of Hurricane Irma from autumn 2017, and the climatology of global precipitation. Using GPM products produced from the DPR and GMI measurements, precipitation and latent heat estimates in three-dimensions are analysed to provide insight into the hurricane's precipitation. Furthermore, the novelty of measurements at two frequencies from the spaceborne precipitation radar are used to analyse the size distribution of precipitation particles (i.e. microphysics) along a cross-section of the hurricane. A combination of the IMERG global-gridded precipitation product and NOAA hurricane data is used to understand how precipitation evolves across the lifetime of a hurricane.

By building on the heritage of the preceding TRMM, the GPM mission now provides a consistent, sub-hourly, high resolution global precipitation record exceeding a 20-year period. A global precipitation climatology, based on the last 20-year IMERG product, has been completed and has been compared with other climatological records from the DWD GPCC gauge product, the GPCP satellite-gauge product, and the ECMWF ERA5 reanalysis.

Such examples epitomise some of the highlights of the GPM mission. The GPM-CO is able to provide information on the precipitation, microphysics and latent heat of precipitating systems, while the GPM constellation of microwave sensors together with infrared sensors and gauges provide rapid updates of surface precipitation (rather than snapshots from individual satellite sensors). GPM precipitation and latent heat estimates have great potential for improving parameterisations in weather forecast, climate and flood prediction models, as well as for near-real-time tracking of extreme events with data available within 2–4h. This paves the way for societal applications such as early warning systems for floods and landslides, and forecast systems for agricultural productivity, famine, and disease outbreaks (Skofronick-Jackson *et al*., 2017). Furthermore, three-dimensional precipitation measurements are critical to improving the representation of Earth system energetics in forecast and climate models, with estimation of latent heat profiles differentiated by precipitation type (stratiform *vs* convective), precipitation rates, precipitation top height and low-level reflectivity gradients that can only be derived by a precipitation radar (Lang and Tao, 2018).

Measuring precipitation has never been as important as in recent times due to climate change, with the projection that extreme events are very likely to increase in number and strength over many regions in the future (IPCC, 2014). The GPM mission advances spaceborne precipitation measurements that are paramount for better understanding and adapting to a changing climate.

Acknowledgements

Daniel Watters was funded by a Natural Environment Research Council studentship awarded through the Central England NERC Training Alliance (CENTA; grant reference NE/L002493/1) and by the University of Leicester. The work by Alessandro Battaglia has been supported by the project 'Radiation and Rainfall' funded by the UK National Centre for Earth Observation (Contract RP18G0002). The version-6B level-3B IMERG (Late and Final Run) data, version-6A level-2B combined DPR-GMI, and CSH data were provided by the NASA/Goddard Space Flight Center and PPS, which develop and compute the data products as a contribution to GPM, and archived at the NASA GES DISC. The GPCP

data were provided by the NOAA/OAR/ESRL PSL, Boulder, Colorado, USA, from their website at https://psl.noaa.gov/. This publication contains modified Copernicus Climate Change Service information (2020); neither the European Commission nor ECMWF is responsible for any use that may be made of the Copernicus information or data it contains. This research used the SPECTRE High Performance Computing Facility at the University of Leicester. The authors thank an anonymous reviewer and Edward Graham for their helpful comments and recommendations that greatly helped to improve the manuscript.

References

Adler RF, **Huffman GJ**, **Chang A *et al***. 2003. The version-2 Global Precipitation Climatology Project (GPCP) monthly precipitation analysis (1979-present). *J. Hydrometeorol.* **4**(6): 1147–1167.

Adler RF, **Sapiano MR**, **Huffman GJ *et al***. 2018. The Global Precipitation Climatology Project (GPCP) monthly analysis (new version 2.3) and a review of 2017 global precipitation. *Atmosphere* **9**(4): 138.

Copernicus Climate Change Service (C3S). 2017. ERA5: Fifth generation of ECMWF atmospheric reanalyses of the global climate, Copernicus Climate Change Service Climate Data Store (CDS). Subset used: January 1979–December 2019. https://cds.climate.copernicus.eu/cdsapp#!/home (accessed 4 May 2020)

GPM Science Team. 2017. GPM DPR and GMI Combined Stratiform Heating L2H 1.5 hours 5 km V06A, Greenbelt, MD, Goddard Earth Sciences Data and Information Services Center (GES DISC). Subset used: 5 September 2017 – Granule 20007. https://doi.org/10.5067/GPM/DPRGMI/CSH/2H/06 (accessed 29 November 2019)

Grecu M, **Olson WS**. 2020. Precipitation retrievals from satellite combined radar and radiometer observations, in *Satellite Precipitation Measurement*. Springer: Cham, Switzerland, pp 231–248.

Hersbach H, **Bell B**, **Berrisford P *et al***. 2020. The ERA5 global reanalysis. *Q. J. R. Meteorol. Soc.* **146**(730): 1999–2049.

Hou AY, **Kakar RK**, **Neeck S *et al***. 2014. The Global Precipitation Measurement mission. *Bull. Am. Meteorol. Soc.* **95**(5): 701–722.

Houze RA Jr. 1997. Stratiform precipitation in regions of convection: a meteorological paradox? *Bull. Am. Meteorol. Soc.* **78**(10): 2179–2196.

Houze RA Jr, **Rasmussen KL**, **Zuluaga MD *et al***. 2015. The variable nature of convection in the tropics and subtropics: a legacy of 16 years of the Tropical Rainfall Measuring Mission satellite. *Rev. Geophys.* **53**(3): 994–1021.

Huffman GJ, **Bolvin DT**, **Braithwaite D *et al.*** 2019a. *NASA Global Precipitation Measurement (GPM) Integrated Multi-satellitE Retrievals for GPM (IMERG). Algorithm theoretical basis document, version 6,* NASA. https://pmm.nasa.gov/sites/default/files/document_files/IMERG_ATBD_V06.pdf (accessed 8 July 2020.)

Huffman GJ, **Stocker EF**, **Bolvin DT *et al.*** 2019b. *GPM IMERG final precipitation L3 half hourly 0.1 degree x 0.1 degree V06B, Greenbelt, MD, Goddard Earth Sciences Data and Information Services Center (GES DISC)*. Subset used: 1 June 2000–31 January 2020. https://doi.org/10.5067/GPM/IMERG/3B-HH/06. (accessed 14 May 2020)

Huffman GJ, **Stocker EF**, **Bolvin DT *et al.*** 2019c. GPM IMERG late precipitation L3 half hourly 0.1 degree x 0.1 degree V06B, Greenbelt, MD, Goddard Earth Sciences Data and Information Services Center (GES DISC). Subset used: 1 February 2020–31 May 2020. https://doi.org/10.5067/GPM/IMERG/3B-HH-L/06. (accessed 3 June 2020)

Huffman GJ, **Bolvin DT**, **Braithwaite D *et al***. 2020. Integrated multi-satellite retrievals for the Global Precipitation Measurement (GPM) Mission (IMERG), in *Satellite Precipitation Measurement*. Springer: Cham, Switzerland, pp 343–353.

IPCC. 2014. in *Climate Change 2014: Synthesis Report. Contribution of Working Groups I, II and III to the Fifth Assessment Report of the Intergovernmental Panel on Climate Change, Core Writing Team*. Pachauri RK, Meyer LA (eds) . IPCC: Geneva, Switzerland.

Kidd C, **Takayabu YN**, **Skofronick-Jackson GM *et al***. 2020. The Global Precipitation Measurement (GPM) mission, in *Satellite Precipitation Measurement*. Springer: Cham, Switzerland, pp 3–23.

Knapp KR, **Kruk MC**, **Levinson DH *et al***. 2010. The international best track archive for climate stewardship (IBTrACS) unifying tropical cyclone data. *Bull. Am. Meteorol. Soc.* **91**(3): 363–376.

Knapp KR, **Diamond HJ**, **Kossin JP *et al.*** 2018. *International best track archive for climate stewardship (IBTrACS) project, version 4, IBTrACS.ALL.v04r00 dataset, NOAA National Centers for Environmental Information*. Subset used: 30 August 2017–13 September 2017. https://doi.org/10.25921/82ty-9e16. (accessed 23 September 2019)

Kummerow C, **Barnes W**, **Kozu T *et al***. 1998. The Tropical Rainfall Measuring Mission (TRMM) sensor package. *J. Atmos. Ocean. Technol.* **15**(3): 809–817.

Lang SE, **Tao W-K**. 2018. The next-generation Goddard convective-stratiform heating algorithm: new tropical and warm-season retrievals for GPM. *J. Clim.* **31**(15): 5997–6026.

Liao L, **Meneghini R**. 2011. A study on the feasibility of dual-wavelength radar for identification of hydrometeor phases. *J. Appl. Meteorol. Climatol.* **50**(2): 449–456.

Meyer-Christoffer A, **Becker A**, **Finger P *et al.*** 2018. *GPCC Climatology Version 2018 at 0.25°: Monthly Land-Surface Precipitation Climatology for Every Month and the Total Year from Rain-Gauges built on GTS-based and Historical Data*. https://doi.org/10.5676/DWD_GPCC/CLIM_M_V2018_025. (accessed 30 April 2020)

Olson WS. 2017. *GPM DPR and GMI combined precipitation L2B 1.5 hours 5 km V06A, Greenbelt, MD, Goddard Earth Sciences Data and Information Services Center (GES DISC)*. Subset used: 5 September 2017 – Granule 20007. https://doi.org/10.5067/GPM/DPRGMI/CMB/2B/06. (accessed 29 November 2019)

Olson WS, **Masunaga H**, **GPM Combined Radar-Radiometer Algorithm Team** 2016. *GPM combined radar-radiometer precipitation. Algorithm theoretical basis document, version 4,* NASA. https://gpm.nasa.gov/sites/default/files/document_files/Combined_algorithm_ATBD.V04.rev_.pdf (accessed 19 February 2020.)

Schneider U, **Becker A**, **Finger P *et al***. 2014. GPCC's new land surface precipitation climatology based on quality-controlled in situ data and its role in quantifying the global water cycle. *Theor. Appl. Climatol.* **115**(1–2): 15–40.

Simpson J, **Kummerow C**, **Tao W-K *et al***. 1996. On the tropical rainfall measuring mission (TRMM). *Meteorog. Atmos. Phys.* **60**(1–3): 19–36.

Skofronick-Jackson G, **Petersen WA**, **Berg W *et al***. 2017. The Global Precipitation Measurement (GPM) mission for science and society. *Bull. Am. Meteorol. Soc.* **98**(8): 1679–1695.

Skofronick-Jackson G, **Kirschbaum D**, **Petersen W *et al***. 2018. The Global Precipitation Measurement (GPM) mission's scientific achievements and societal contributions: reviewing four years of advanced rain and snow observations. *Q. J. R. Meteorol. Soc.* **144**(S1): 27–48.

Wang JJ. 2018. *GPCP version 2.3 combined precipitation data set, NOAA's Physical Sciences Laboratory*. Subset used: January 1979 – December 2019. https://psl.noaa.gov/data/gridded/data.gpcp.html#restrict (accessed 30 April 2020.)

Watters D, **Battaglia A**. 2020. The NASA-JAXA Global Precipitation Measurement mission – part I: New frontiers in precipitation. *Weather* https://doi.org/10.1002/wea.3865.

Correspondence to: D. Watters

dcw17@leicester.ac.uk

doi: 10.1002/wea.3869